



## Numerical study of structure parameters on energy transfer and flow characteristics of integrated energy recovery and pressure boost device

Fang-long Yin, Song-lin Nie \*, Hui Ji, Fang-li Lou

Beijing Key Laboratory of Advanced Manufacturing Technology, Beijing University of Technology, Beijing 100124, China, email: yfl@bjut.edu.cn (F.-l. Yin), Tel. +86 10 67396362, Fax +86 10 67391617, email: niesonglin@bjut.edu.cn (S.-l. Nie), jihui1310@163.com (H. Ji), loufangli2017@163.com (F.-l. Lou)

Received 3 November 2017; Accepted 25 August 2018

### ABSTRACT

Energy recovery device (ERD) is a critical power component in seawater reverse osmosis (SWRO) desalination system. In this study, the energy transfer and flow characteristics for an innovative integrated energy recovery and pressure boost device (IERPBD) are investigated. The IERPBD which consists of a rotary pressure exchanger (RPE) and an axial piston type booster pump (APBP) is introduced in Section 2. To optimize both the structure parameters and working conditions of IERPBD, a series of three-dimensional (3D) CFD simulations are carried out. The CFD simulations for the RPE with port plate silencing grooves are conducted with a set of operating conditions through orthogonal designed theory. It should be noted that the leakage through the lubricating gaps of valve-port plate, fluid compressibility effect and cavitation damage are considered in the simulation. And partial numerical results are validated by comparison with the results from other research groups. The mixing process, pressure distribution, components distribution, leakage flow characteristics and related characteristic parameters of RPE are presented in Section 3. And then the optimal parameters of RPE with a duct diameter of 10 mm, duct length of 70 mm, 12 ducts with fresh seawater flow of 10.8 L/min were used to design the IERPBD. The energy transfer and flow characteristics of IERPBD were also presented with different gap heights of the valve-port plate interface. The simulation results turned out that when the lubricating gap height of valve-port plate changes from 5  $\mu\text{m}$  to 20  $\mu\text{m}$ , the flow ripple rate of RPE could increase from 6.15% to 36.13%, whereas the energy recovery efficiency of RPE could decrease from 97.2% to 49.8%. Therefore, a well-designed lubricating gap of valve-port plate could improve both energy transfer and flow characteristics of IERPBD. This research will lay the foundation for the further development of high efficiency and low fluid noise IERPBD.

*Keywords:* Energy recovery; Flow characteristics; Numerical simulation; Orthogonal design; Reverse osmosis desalination

### 1. Introduction

The worldwide consumption of drinking water doubles every 20 years. Since only 1% of Earth's water is drinkable, seawater desalination technology is widely used to produce potable water from the sea. Seawater reverse osmosis (SWRO) desalination has emerged as a preferred method for purifying seawater. This technology is simple, compact, low investment, and requires less energy than other desali-

nation techniques [1–5]. Wherever people need to purify water for drinking, SWRO desalination technology plays an increasingly important role. The energy recovery device (ERD) is a critical component in the SWRO system, which can effectively recover the pressure energy from the rejected high-pressure brine and reduce the operational costs [6–8]. The rotary pressure exchanger (RPE) is a kind of isobaric ERD following the positive displacement principle, which could directly transfer the energy from high-pressure brine to low pressure seawater and achieve high energy recovery efficiency [9].

\*Corresponding author.

To investigate the energy transfer characteristics and working mechanism of the ERD, many research efforts have been made on the mixing process and flow characteristics of the RPE by computational fluid dynamics (CFD) simulation. Zhou et al. [10] and Liu et al. [11] presented 2D and 3D CFD simulations for studying the dynamic mixing process and the effects of rotation speed and the flow rate on the volumetric mixing rate of the RPE, respectively. Zhao et al. [12] studied the pressure ripple characteristics of RPE outlets by 3D CFD simulation. It was shown that the dominant frequency of the pressure fluctuation is the channel passing frequency. Yuan et al. [13] researched the pulsating and mixing characteristics of RPE by a 2D unsteady numerical model, and an optimal Strouhal number was presented. Wang et al. [14] numerically investigated the mixing process and concentration distribution of the RPE with different sizes and structures of the end cover. Cao et al. [15] studied the effects of extended angle and operating condition on the volumetric mixing rate and flow pattern of RPE. Wang and Xu [16] numerically and experimentally investigated the effects of operational conditions on the mixing behavior of a four-port RPE. Later, they also studied the applicability of hydrostatic bearing technology and pre-pressurization and depressurization grooves in RPE by CFD simulation and validating experiment [17,18]. It was concluded that the hydrostatic bearing structure could improve the lubricating characteristic and service life of RPE, and the flow fluctuations of the RPE could effectively be reduced by using the pre-pressurization and depressurization grooves. In another research [19], they investigated numerically and experimentally the rotor speed for a self-driven RPE, and a theoretical formula for calculating the theoretical rotating speed of the rotor was obtained.

In recent years, several attempts have been pursued to improve the energy recovery efficiency of RPE. Stover [20] was devoted to studying the pressure-transfer efficiency of RPE. It was discovered that about 5% pressure transfer efficiency was lost due to the compression of the seawater, viscous friction and internal leakage. Wu et al. [21] put forward some detailed investigations on the internal leakage, lubrication properties and support mechanism of the simulated end gap in RPE. Wu and Wang [22] focused on improving dynamic seal performance of the RPE by making textured grooves on the surfaces of two end covers. The experimental results showed that the energy recovery efficiency of RPE could be increased up to 96.3%. Wu et al. [23] introduced a theoretical analysis for the optimization of energy recovery efficiency, and auxiliary experiments were completed to determine the optimal processing capacity for a specific RPE.

Generally, a booster pump is essentially employed after the RPE to compensate the pressure loss in the REP and RO membrane modules to satisfy the operating pressure needs of the desalting system [24]. And most of the booster pump and the RPE are arranged independently. Recently, integrated energy recovery and pressure boost device (IERPBD) i Save was presented by Danfoss Company [25]. The i Save consists of a rotating isobaric pressure exchanger and a vane type booster pump, and the pressure exchanger and the pump are driven by the same

electric motor. However, it has been demonstrated that the leakage of seawater hydraulic vane pump is slightly high, and the volumetric efficiency of seawater hydraulic vane pump is lower than seawater hydraulic axial piston pump [2]. In order to solve this problem and further improve the efficiency of IERPBD, an innovative IERPBD consisting of a rotary pressure exchanger (RPE) and an axial piston type booster pump (APBP) was presented in this study. Although extensive work has been conducted to study the mixing process, flow characteristics, optimization design and improvement of energy recovery efficiency of RPEs, very few numerical simulations are reported to reveal the effects of structure parameters and working conditions on flow and energy loss characteristics of IERPBD. Therefore, it is important to numerically optimize both the structure parameters and working conditions of IERPBD. Besides, as discussed by Wu et al. [22], the interface between the valve plate and port plate is crucial in IERPBD as most of the leakage and frictional loss are generated through the interface, which would result in a significant influence on the efficiency, performance, and reliability of IERPBD. It is also necessary to point out that most of the previous 3D CFD simulation studies presented have neglected the leakage in the REP lubricating gaps. Therefore, in this paper, the leakage of the valve-port plate pair is one of the essential issues that need to be considered during the numerical simulation of IERPBD.

The objective of this research is to investigate the mixing process, flow and pressure characteristics of a newly designed IERPBD with different structure parameters (duct diameter, duct length, number of ducts and valve-port plate gap heights) and working conditions (fresh seawater flow). Therefore, both the structure parameters and working conditions of IERPBD will be optimized. The developed CFD model firstly included the silencing grooves on the port plate, lubricating gaps in the valve-port plate interface. In addition, the effects of fluid compressibility and cavitation are considered inside IERPBD. Section 2 introduced the working principle and mathematical model of IERPBD, as well as the numerical solution procedure. By using the orthogonal design, numerical results and analyses of the RPE and IERPBD with different sensitive factors are presented in Section 3, and the optimal structure parameters and working conditions of IERPBD are obtained. Conclusions are presented in Section 4.

## 2. Theoretical description

### 2.1. Description of IERPBD

Fig. 1 displays the configuration of the innovative IERPBD, which is composed of a rotary pressure exchanger (RPE) and an axial piston type booster pump (APBP). The structure of proposed IERPBD is different from the existed IERPBD product i Save, which consists of a rotating isobaric pressure exchanger and a vane type booster pump [25]. The RPE contains two port plates, the one at the brine side and the other one at the seawater side. Between the two port plates, there is a rotor with several ducts connecting the brine side with the seawater side. When the driven shaft rotates counterclockwise, the RPE transfers pressure from the high-pressure brine inlet (HPB in) to the low-pressure

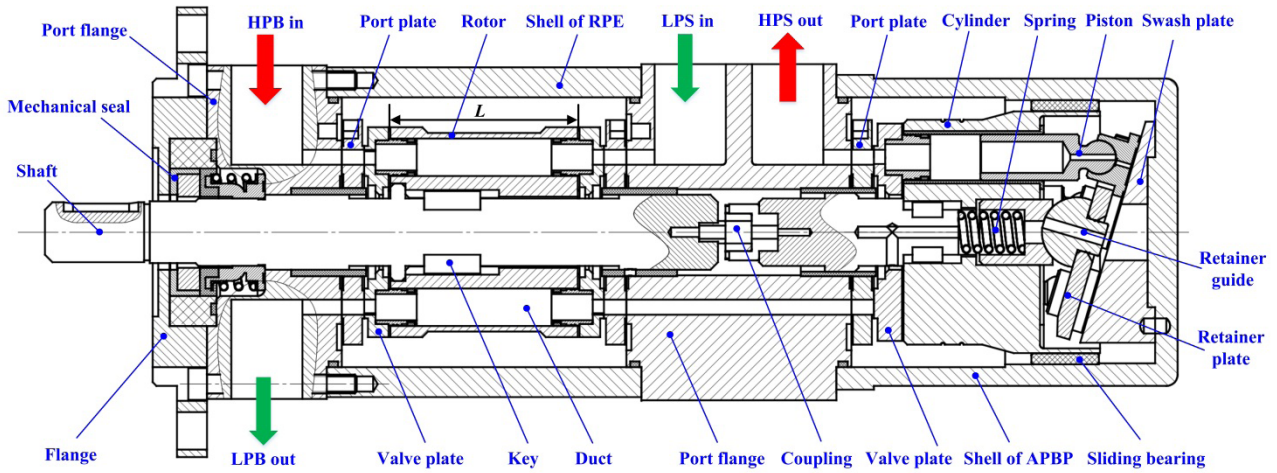


Fig. 1. Configurations of the IERPBD.

seawater that flows from the low-pressure inlet (LPS in). When the high-pressure brine flows into the RPE, it pressurizes the sea water in the duct that flows from “LPS in”. The pressurized seawater is then pumped to the intake port of the APBP. Moreover, the low-pressure brine could be pushed out of the low-pressure outlet (LPB out) of RPE by the pressurized seawater. Because there is no physical barrier in the ducts between the brine and seawater, there will be a small amount of mixing between the two liquids in the ducts of the RPE, therefore slightly reducing the pressure of the pressurized seawater. As the piston in the APBP passes over the intake port, it starts to move toward the swash plate, and the seawater rushes into the piston chamber through the intake port. This intake continues until the piston reaches top dead center (TDC) of the port plate in APBP [28]. When the piston reaches the top dead center (TDC) of the port plate in APBP, it is supposed to discharge seawater into the discharge port. When the piston passes over the discharge port, it advances into the cylinder hole, and the seawater is pushed out of the high-pressure seawater outlet (HPS out) of APBP. During this process, the pressure of pressurized seawater could be increased, and APBP could compensate the pressure loss during the energy transfer process in the RPE.

## 2.2. Mathematical model

### 2.2.1. Target parameters

The maximum rotor inflow length  $l_{max}$ , the volumetric efficiency of the duct  $\eta$ , volumetric mixing  $\phi$  and energy recovery efficiency  $E$  are essential parameters of IERPBD. During the development phase of IERPBD, the  $l_{max}$  should be taken into account. If the  $l_{max}$  is too small, the device will not be able to obtain an effective pressure exchange. Otherwise, if the  $l_{max}$  is too large, the volumetric efficiency of the device will be reduced. During the pressure transition processes, the  $l_{max}$  can be calculated by using the following formula [10]:

$$l_{max} = \int_{t_0}^{t_0 + \frac{T}{2}} v_{mix}(t) dt \quad (1)$$

where  $t_0$  is the sealing time of the duct,  $T$  is the rotating period of the rotor, and  $v_{mix}(t)$  is the velocity of the fluid in the duct.

The volumetric efficiency of the duct  $\eta$ , which could characterize the amount of the pressurized seawater during the rotating period of the rotor, can be given by [11]

$$\eta = \frac{l_{max}}{L} \quad (2)$$

where  $L$  is the length of the duct (as illustrated in Fig. 1).

As is known, the volumetric mixing ratio  $\phi$  is an important parameter for evaluating the mixing degree in IERPBD, which can be expressed as [10,14,15]

$$\phi = \frac{C_{HP-out} - C_{LP-in}}{C_{HP-in} - C_{LP-in}} \times 100\% \quad (3)$$

where  $C_{HP-out}$  is the salinity of the pressurized sea water at the high-pressure outlet,  $C_{LP-in}$  is the salinity of fresh seawater at the low pressure inlet, and  $C_{HP-in}$  represents the salinity of the incoming brine at the high pressure inlet.

Besides, the energy recovery efficiency  $E$  is an important index to measure the energy conservation efficiency of the IERPBD. By integrating the pressure and flow of the pressurized seawater, high-pressure brine and fresh seawater, the energy recovery efficiency  $E$  can be presented as [22]

$$E = \frac{P_{HP-out} \times Q_{HP-out} + P_{LP-out} \times Q_{LP-out}}{P_{HP-in} \times Q_{HP-in} + P_{LP-in} \times Q_{LP-in}} \quad (4)$$

where  $P_{HP-out}$ ,  $P_{HP-in}$ ,  $P_{LP-in}$  and  $P_{LP-in}$  are the pressure of pressurized seawater at the high-pressure outlet, the pressure of high-pressure brine at the high-pressure inlet, the pressure of low-pressure brine at low-pressure outlet and the pressure of the fresh seawater at the low-pressure inlet, respectively. Moreover,  $Q_{HP-out}$ ,  $Q_{HP-in}$ ,  $Q_{LP-out}$  and  $Q_{LP-in}$  denote the flow of pressurized seawater at the high-pressure outlet, the flow of high-pressure brine at the high-pressure inlet, the flow of low-pressure brine at low-pressure outlet and the flow of the fresh seawater at the low-pressure inlet, respectively.

### 2.2.2. The temporal pressure inside the duct

The temporal pressure inside each piston can be found by applying the continuity equation in integral form in the duct, as given in Eq. (5) [29]

$$\frac{dP_d}{dt} = \frac{K_c}{V} (q_i - q_l) \quad (5)$$

where  $P_d$  is the temporal pressure inside the duct,  $K_c$  is the bulk modulus of the fluid,  $V$  is the temporal volume of the duct,  $q_i$  is the reverse flow through the silencing groove, and  $q_l$  is the leakage flow across the gap between the valve plate and port plate.

At top dead center, when the piston is entering the discharge port, the water in the discharge port may flow into the duct reversely, until the fluid pressure within the piston chamber is equal to that in the discharge port. The reverse flow  $q_i$  can be written as follows [29]

$$q_i = C_i A_i \sqrt{\frac{\rho}{2} |P_d - P_o| \cdot \text{sign}(P_d - P_o)} \quad (6)$$

where  $C_i$  is the discharge coefficient of the silencing groove,  $A_i$  is the flow area of the silencing groove,  $P_o$  is the outlet pressure at the high-pressure outlet, and  $\rho$  is the density of the fluid.

### 2.2.3. Governing equations for CFD simulation

The conservation equations of mass, momentum and energy are the fundamental equations of the CFD simulation. In this research, the heat transfer in IERPBD is not included, and the temperature distribution of fluid within the numerical model is neglected. Therefore, the basic continuity, momentum and component equations can be given in Eqs. (7)–(9), respectively [30].

$$\frac{\partial}{\partial t} \int_{\Omega(t)} \rho d\Omega + \int_{\sigma} \rho (\mathbf{v} - \mathbf{v}_\sigma) \cdot \mathbf{n} d\sigma = 0 \quad (7)$$

$$\frac{\partial}{\partial t} \int_{\Omega(t)} \rho \mathbf{v} d\Omega + \int_{\sigma} \rho ((\mathbf{v} - \mathbf{v}_\sigma) \cdot \mathbf{n}) \mathbf{v} d\sigma = \int_{\sigma} \tilde{\boldsymbol{\tau}} \cdot \mathbf{n} d\sigma - \int_{\sigma} p \mathbf{n} d\sigma + \int_{\sigma} \mathbf{f} d\sigma \quad (8)$$

$$\frac{\partial (c_s)}{\partial t} + \frac{\partial (c_s v_r)}{\partial r} + \frac{\partial (c_s v_\theta)}{\partial \theta} + \frac{\partial (c_s v_z)}{\partial z} = \frac{\partial}{\partial r} \left( D_s \frac{\partial c_s}{\partial r} \right) + \frac{\partial}{\partial \theta} \left( D_s \frac{\partial c_s}{\partial \theta} \right) + \frac{\partial}{\partial z} \left( D_s \frac{\partial c_s}{\partial z} \right) \quad (9)$$

where  $\Omega(t)$  is the control volume,  $\sigma$  is the surface area of control volume,  $\rho$  is the fluid density,  $\mathbf{v}$  is the fluid velocity vector,  $\mathbf{v}_\sigma$  is the surface motion velocity vector,  $\mathbf{n}$  is the normal vector of point on surface,  $p$  is the fluid pressure,  $\mathbf{f}$  is the body force,  $c_s$  is volume concentration of the component, and  $D_s$  is diffusion coefficient of the component. It is assumed that the seawater is Newtonian, and the shear stress tensor  $\boldsymbol{\tau}$  can be defined as [31]

$$\tau_{ij} = \mu \left( \frac{\partial u_i}{\partial x_j} + \frac{\partial u_j}{\partial x_i} \right) - \frac{2}{3} \mu \frac{\partial u_k}{\partial x_k} \delta_{ij} \quad (10)$$

where  $\delta_{ij}$  is the Kronecker delta function, and  $u_i$  ( $i = 1, 2, 3$ ) is a component of velocity  $\mathbf{v}$ .

## 2.3. Numerical simulation

### 2.3.1. CFD model

The Computational Fluid Dynamics (CFD) analysis was performed through the commercial CFD software Pump Linx 4.0 to investigate the influence of structure and operating parameters on the energy transfer and flow characteristics of the RPE and IERPBD. The CFD simulation was divided into two stages. Firstly, based on the orthogonal design theory, the CFD simulation of REP has been conducted to optimize its structure and operating parameters, including duct diameter, duct length, number of ducts, gap heights of the valve-port plate and fresh seawater flow. Then the optimal parameters were used to design the REP, and a whole CFD simulation of IERPBD was presented with different gap heights of the valve-port plate interface. The use of the silencing groove on the port plate is an effective method to reduce the pressure pulsations of the RPE and APBP [17,23]. In the CFD simulation model, the silencing grooves were respectively located in the pre-compression zone and pre-relief zone of the port plate. Since the numerical study in this paper was conducted via CFD simulation, it is difficult to consider the effects of port plate tilt in the whole RPE or IERPBD fluid domains. Thus, in this research, the lubricating gaps and gap heights between valve-port plate are supposed as constant in the simulation model.

The flow chart for the CFD simulation by using Pump Linx is depicted in Fig. 2. Firstly, the fluid domain of the RPE and IERPBD were subtracted from CAD geometry and divided into several volumes and meshed separately. And then two types of meshes were created in the Pump Linx. For special moving components such as the ducts and pistons, the rotor template mesher is used to create an optimized mesh specifically for the component geometry. Those independent volumes were connected through sliding interfaces during simulation. For all other parts of the fluid domain, the general mesher is used to create a body-fitted binary tree mesh. And the annulus mesh of the valve-port plate gap was created by the template mesher. To ensure that the flow characteristics in the valve-port plate gap could be presented precisely, as shown in Fig. 3, the number of mesh layers in the valve-port plate gap is ten. Fig. 3 shows the whole computational grid model of the RPE and IERPBD with lubricating gaps, respectively. Taking advantage of the speed ability of the Pump Linx, using a quasi-steady multi-reference frame (MRF) technique, full transient simulations were also performed to investigate the potential effects of any pulsations on the performance [30], which significantly improves the accuracy of the simulation. The convergence criterion of the simulation is set to 0.1. The relaxation of velocity and pressure are both set to 0.45. The second order time accuracy and second order upwind numerical scheme are employed for the numerical simulation. Moreover, the SIMPLEC method is applied to the pressure velocity coupling. To simulate the mixing process and component distribution, the water bulk modulus is defined and the cavitation module is selected in the CFD software in pre-processing of the simulation.

### 2.3.2. Orthogonal design for the RPE CFD simulation

Generally, the flow characteristics of RPE are influenced by the structure and operating parameters such as the duct

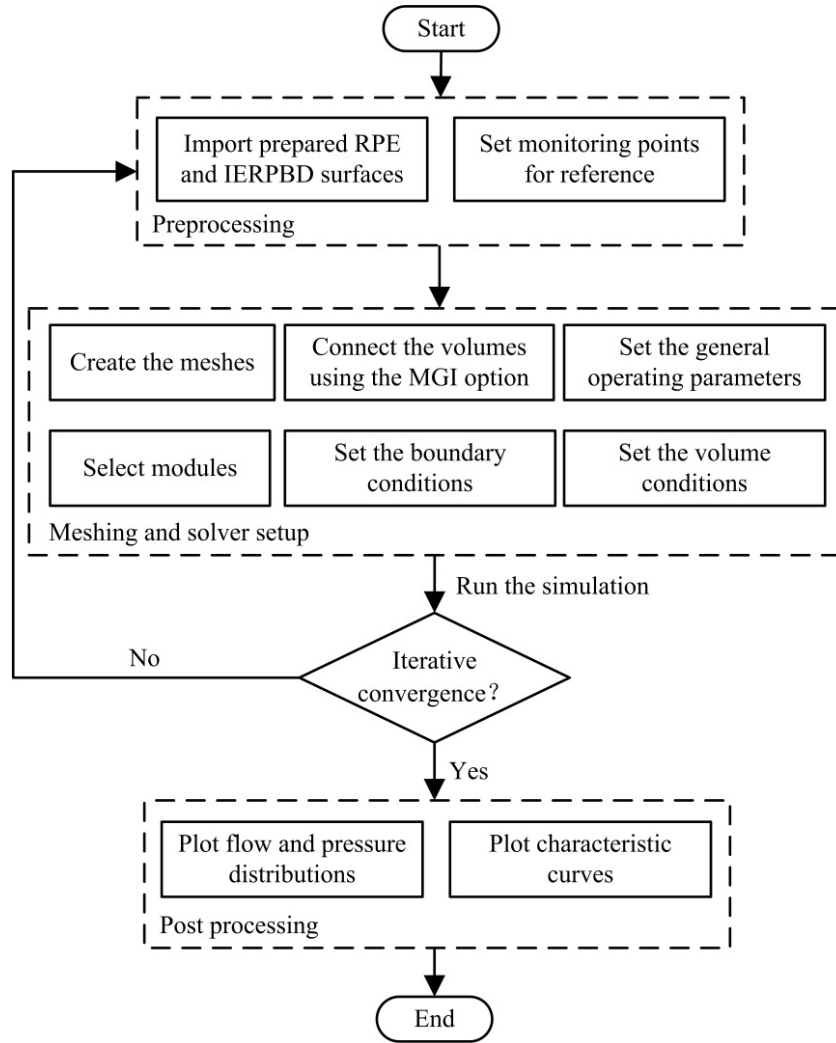


Fig. 2. Flow chart for CFD simulation.

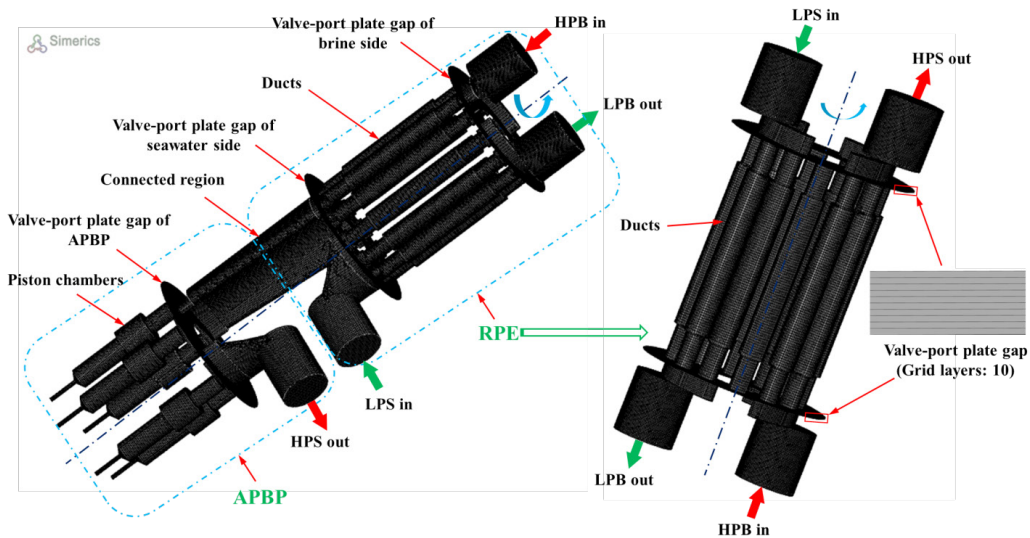


Fig. 3. Mesh model of IERPBD and RPE for CFD simulation.

diameter  $d$ , duct length  $L$ , number of ducts  $N$ , fresh seawater flow  $Q_{LP-in}$ . The principle and the method of orthogonal designed conditions listed in Table 1 are used for determining the main design parameters of RPE. Then the optimal structure parameters and working conditions of RPE can be obtained with a minimum of experiment times, and an  $L_{16}$  ( $4^4$ ) orthogonal table is presented in Table 2. The assignment of proper boundary conditions plays a crucial role in CFD simulation. Moreover, the numerical analysis is performed based on the operating conditions listed in Table 3.

### 3. Results and discussion

Since it is impossible to include all of the flow characteristics result here, some representative outcomes, including the mixing process, pressure distribution, flow and pressure characteristics are explicated to demonstrate the essential findings. Because the structure form and parameters of the developed IERPBD are different from other similar exiting energy recovery devices, it is difficult to make direct comparison between the data results of IERPBD and other exiting energy recovery devices. Therefore, partial numerical results of the RPE are compared with the results from other research groups.

#### 3.1. Mixing process and pressure distributions of IERPBD

Figs. 4 and 5 show the simulated components and pressure distributions in the RPE and IERPBD with the boundary conditions listed in Table 4, and the valve-port plate gap height  $\delta$  of 10 microns with silencing grooves. To validate the simulation results of components distribution in the RPE, comparisons were made between the proposed model and the studies by Liu et al. [11]. Because the heat transfer in IERPBD is not included in this research, the fluid temperature is assumed to be the initial value (20°C). As shown in Fig. 4a, the low-pressure seawater side of the flow field is very clearly marked as the blue region, and the high-pressure brine side is marked as the red region, and the rest represents the mixing section of the seawater and brine. It is clear that the fluid piston is located in the middle of the duct, and the distribution of the components at the same location for each duct was essentially unchanged. It is noticed from Fig. 4a that a mixing section was formed in the duct, and the length and state of the mixing section were nearly unchanged in the REP. Fig. 4b illustrates the components distribution of RPE simulated by Liu et al. [11]. It can be seen that the components distribution of ducts calculated by the proposed CFD model consistent with the results of Liu et al. As shown in Fig. 4c, when the duct reaches the discharge port of the port plate by passing over the pre-compression zone and completes the suction process, the seawater pressures inside the duct and the lubricating gap begin to rise, so the energy from the high-pressure brine is transferred to the seawater. Because of the leakage through the valve-port plate gap, it can be seen (through the gradient colors) that, the pressure inside the port plate gap of the high-pressure zone is gradually reduced. Fig. 4c also clearly shows the reversed flow as the piston is connected to the silencing groove. According to Manring and Zhang [32], as the duct passes over

Table 1  
Factors and levels of orthogonal design

Number	Factors	Levels			
		1	2	3	4
1	Duct diameter $d$ (mm)	6	8	10	12
2	Duct length $L$ (mm)	50	60	70	80
3	Number of ducts $N$	6	8	10	12
4	Fresh seawater flow $Q_{LP-in}$ (L·min <sup>-1</sup> )	10.2	10.8	11.4	12.0

Table 2  
Orthogonal design data

Number	Duct diameter $d$ (mm)	Duct length $L$ (mm)	Number of ducts $N$	Fresh seawater flow $Q_{LP-in}$ (L·min <sup>-1</sup> )
1	6	50	6	10.2
2	6	60	8	10.8
3	6	70	10	11.4
4	6	80	12	12.0
5	8	50	8	11.4
6	8	60	6	12.0
7	8	70	12	10.2
8	8	80	10	10.8
9	10	50	10	12.0
10	10	60	12	11.4
11	10	70	6	10.8
12	10	80	8	10.2
13	12	50	12	10.8
14	12	60	10	10.2
15	12	70	8	12.0
16	12	80	6	11.4

Table 3  
Parameters for computational fluid dynamics (CFD) analysis

Description	Symbol	Value	Unit
Dynamic viscosity of brine	$\mu_1$	$1.09 \times 10^{-3}$	Pa·s
Dynamic viscosity of seawater	$\mu_2$	$1.05 \times 10^{-3}$	Pa·s
Density of brine	$\rho_1$	$1.025 \times 10^3$	Kg/m <sup>3</sup>
Density of seawater	$\rho_2$	$1.013 \times 10^3$	Kg/m <sup>3</sup>
Operating Temperature	$T_i$	20	°C
Rotational speed	$n$	1500	r/min

the TDC of the port plate reaching the pre-compression zone, the fluid in the discharge port would flow through the silencing groove into the duct until the duct pressure is equal to that inside the chamber of HPS out. To make these pressures equal, the fluid in the duct would be compressed, and the energy from the discharge port should be transferred to the duct. Owing to this intermittent pulse of the reversed flow, the volumetric efficiency of the duct  $\eta$  should be reduced. A similar phenomenon has been pre-

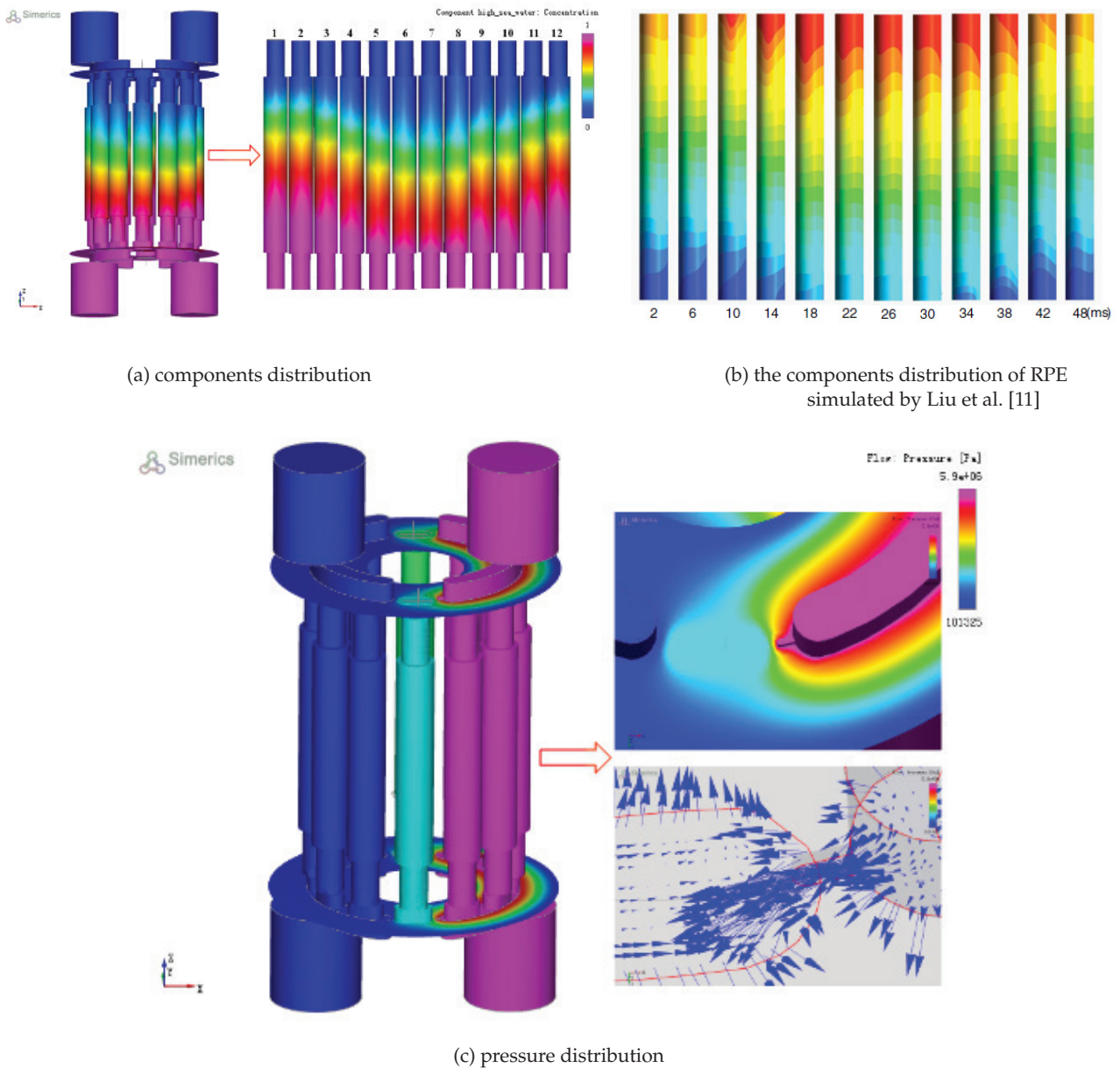


Fig. 4. Components and pressure distributions of RPE. (a) components distribution, (b) the components distribution of RPE simulated by Liu et al. [11], (c) pressure distribution.

viously reported by literature [28]. It can be seen from Fig. 5a that the components distribution of RPE in IERPBD is nearly similar to the previous analysis results. The fluid piston keeps in the middle of the duct, and the distribution of the components at the same location remains substantially constant. It is evident from Fig. 5a that the APBP is filled with pressurized seawater, and there is nearly no high-pressure brine in the discharge port of the APBP. In Fig. 5b it is observed that as the duct connecting with the port of RPE, the pressure from the high-pressure brine was immediately transferred to the seawater by high speed inter-collision of the fluid, and the pressure on the valve-port plate gap in the high-pressure zone is also gradually reduced. It is noticed that the APBP increased the pressure

of the pressurized seawater, and the pressure difference between the intake and the discharge port of the APBP is about 1.1 MPa.

### 3.2. Effect of structure and operating parameters on target parameters

Fig. 6 illustrates the maximum rotor inflow length of the RPE  $l_{max}$  with different structure and operating parameters  $d$ ,  $L$ ,  $N$ , and  $Q_{LP-m}$ . It is clearly shown in Fig. 6 that the  $l_{max}$  is decreasing with the increase of  $d$ ,  $L$ , and  $N$ , and the  $l_{max}$  reaches the maximum value when the  $Q_{LP-m}$  is 10.8 L/min. The volumetric efficiency of the duct  $\eta$  with different  $d$ ,  $L$ ,

$N$  and  $Q_{LP-in}$  are plotted in Fig. 7. It is evident from Fig. 7 that the  $\eta$  is also decreasing with the increase of  $d$ ,  $L$  and  $N$ , and the  $\eta$  reaches the highest under the  $Q_{LP-in}$  of 10.8 L/min. In comparisons with Fig. 6 and Fig. 7, it is obvious that an

Table 4  
Results of orthogonal design simulation

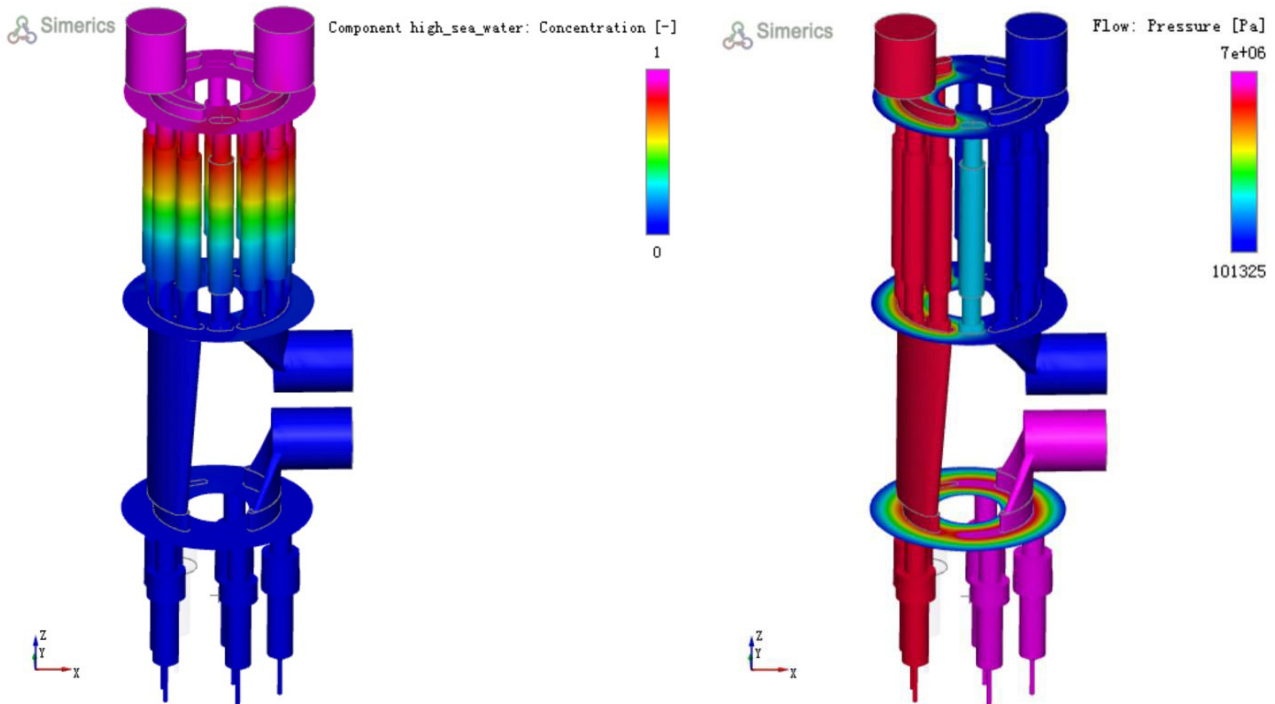
Number	Maximum rotor inflow length $l_{max}$ (mm)	Duct volumetric efficiency $\eta$ (%)	Volumetric mixing $\phi$ (%)
1	177.169	3.543	99.9%
2	140.693	2.345	99.9%
3	118.807	1.697	99.8%
4	104.217	1.303	99.3%
5	83.536	1.671	99.7%
6	117.244	1.954	99.8%
7	49.829	0.712	10.6%
8	63.312	0.791	11.5%
9	45.022	0.900	14.2%
10	35.642	0.594	1.95%
11	67.533	0.965	16.7%
12	47.836	0.598	1.96%
13	infeasible	infeasible	infeasible
14	26.575	0.443	1.54%
15	39.081	0.558	1.88%
16	49.503	0.619	2.02%

excessive  $l_{max}$  could make the  $\eta$  exceed 1. It can be described to that, as the  $\eta$  exceed 1, the mixing zone and brine could be pushed out of the duct, and then the pressurized sea water is easily polluted. To validate the simulation results, comparisons were also made between the proposed model and the studies by Liu et al. [11]. Fig. 8a reports the volumetric mixing  $\phi$  with different  $d$ ,  $L$ ,  $N$  and  $Q_{LP-in}$ . It can be seen from Fig. 8a that the  $\phi$  gradually decreases with the increase of  $d$ ,  $L$  and  $N$ . However, with the increase of the  $Q_{LP-in}$ , the  $\phi$  decreases, which is consistent with the calculation result drawn by Liu et al. (as shown in Fig. 8b).

Table 4 presents the results of orthogonal design simulation. It should be noted that the thirteenth test results are infeasible. It is noteworthy from Table 4 that, the high volumetric efficiency of the duct  $\eta$  could increase the volumetric mixing  $\phi$ . Based on the simulation results, to increase the  $\eta$  and reduce the  $\phi$  as much as possible, the optimal structure and operating parameters of the REP are  $d = 10$  mm,  $L = 70$  mm,  $N = 12$  and  $Q_{LP-in} = 10.8$  L/min, respectively.

3.3. Effect of gap heights between valve-port plates on energy transfer and flow characteristics

Fig. 9a depicts the pressure inside the duct  $p_d$  versus simulation time with different gap heights of the valve-port plate interface. The operating conditions are: the rotational speed of 1500 rpm,  $Q_{LP-in}$  of 10.8 L/min and  $Q_{HP-in}$  of 12.0 L/min, respectively. Here four different valve-port plate gap heights of 5  $\mu$ m, 10  $\mu$ m, 15  $\mu$ m and 20  $\mu$ m are considered. As shown in Fig. 9a, during the pressure build-up stage (0–2 ms), the rising velocity of the pressure inside the duct tends



(a) Components distribution of IERPBD

(b) Pressure distribution of IERPBD

Fig. 5. Components and pressure distributions of IERPBD.

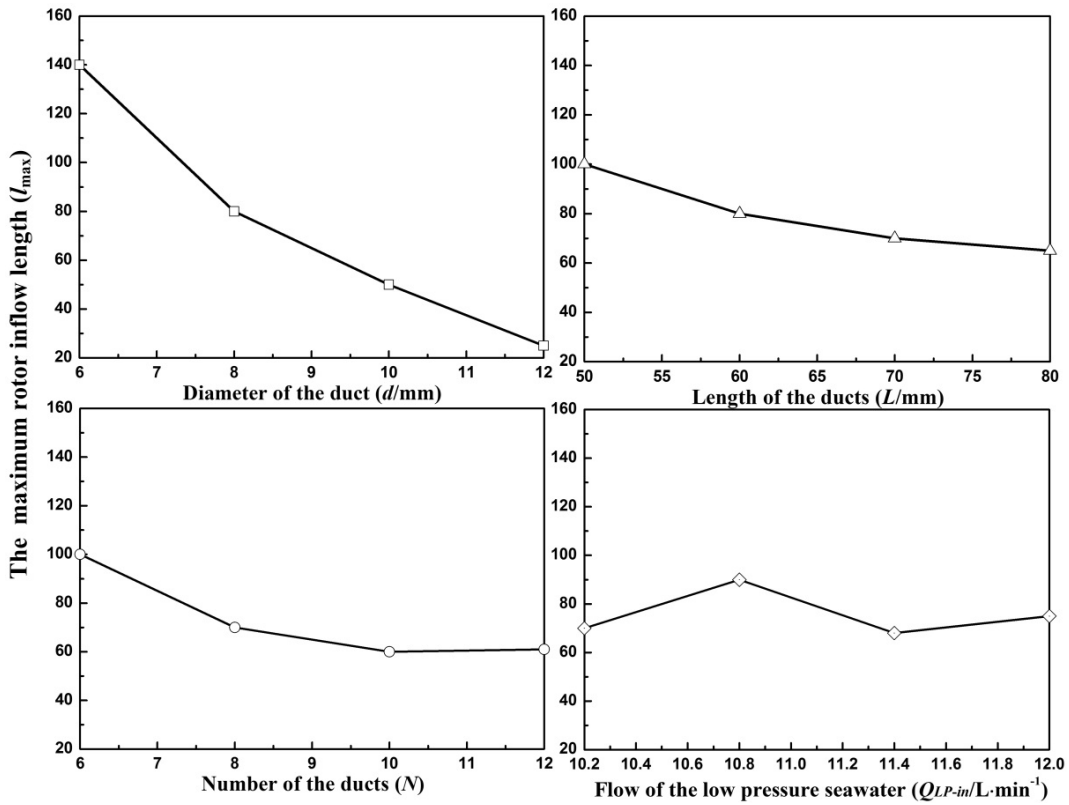


Fig. 6. Maximum rotor inflow length of the RPE with different orthogonal parameters.

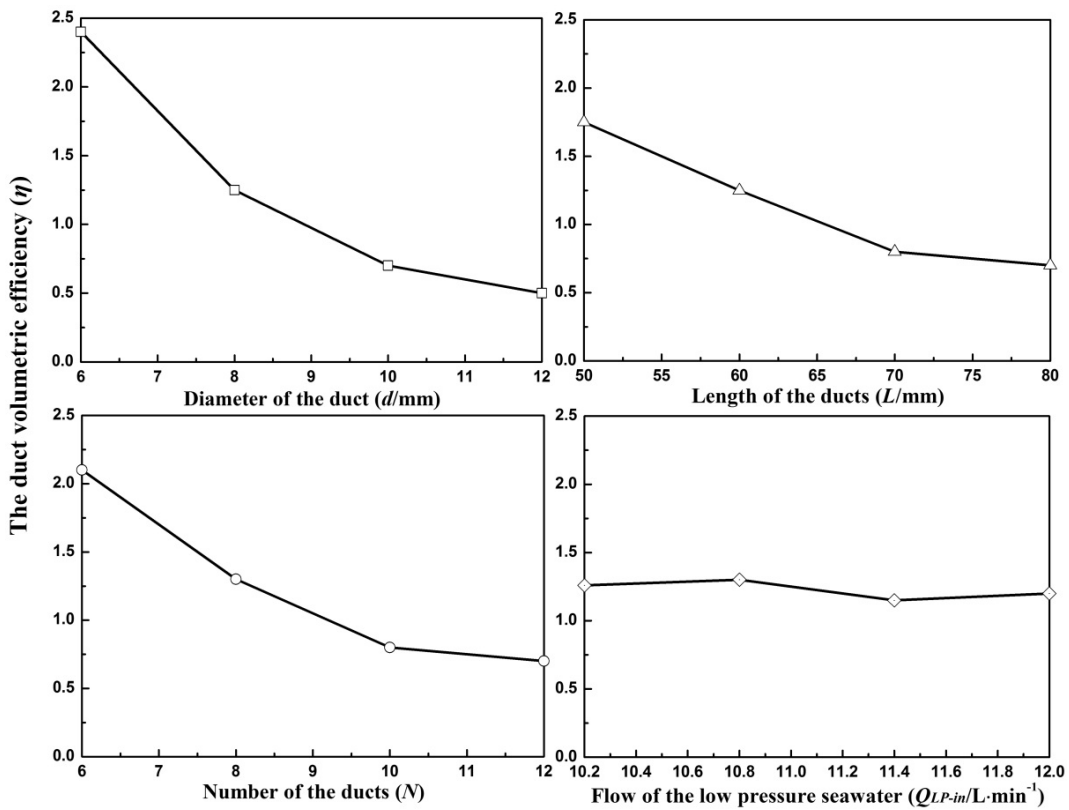
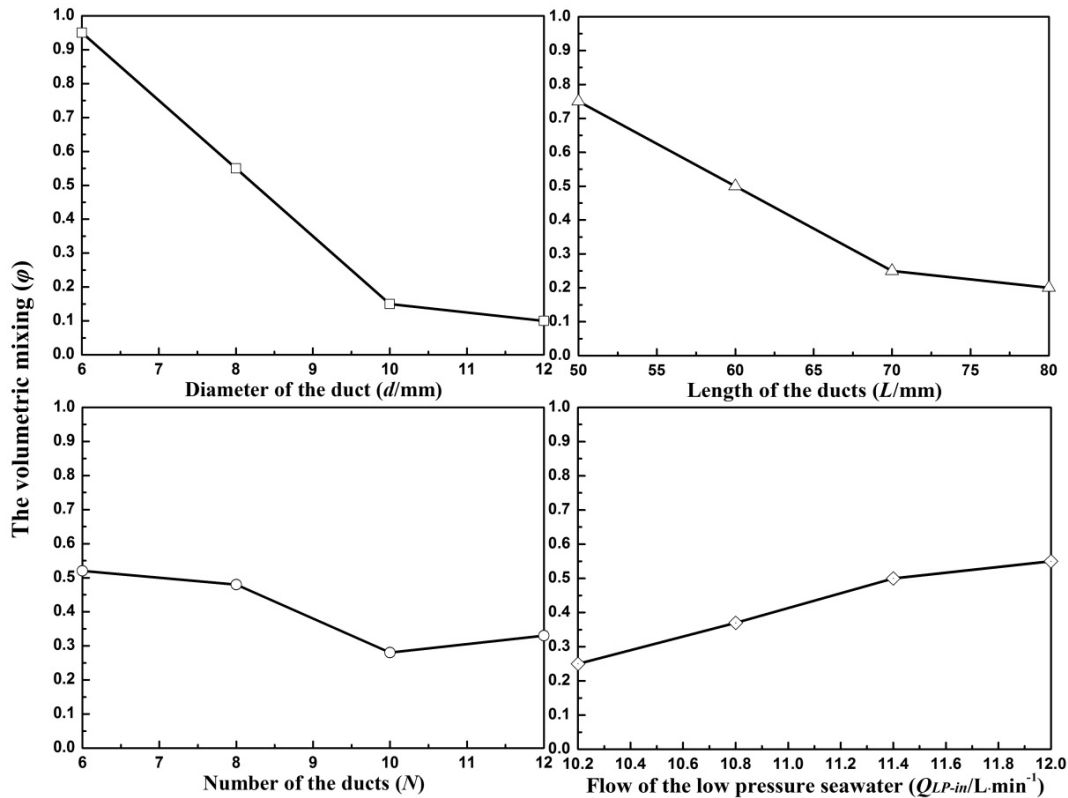
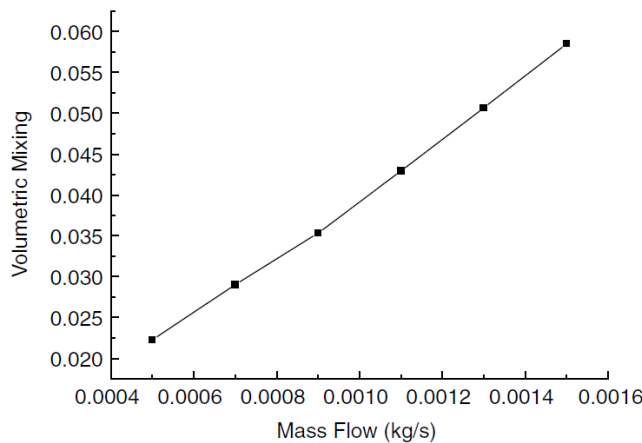


Fig. 7. Duct volumetric efficiency of the RPE with different orthogonal parameters.



(a) volumetric mixing with different orthogonal parameters

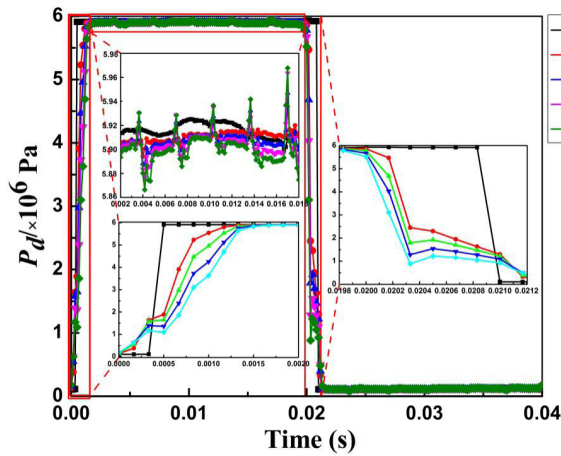


(b) relationship between  $Q_{LP-in}$  and volumetric mixing by Liu et al. [11]

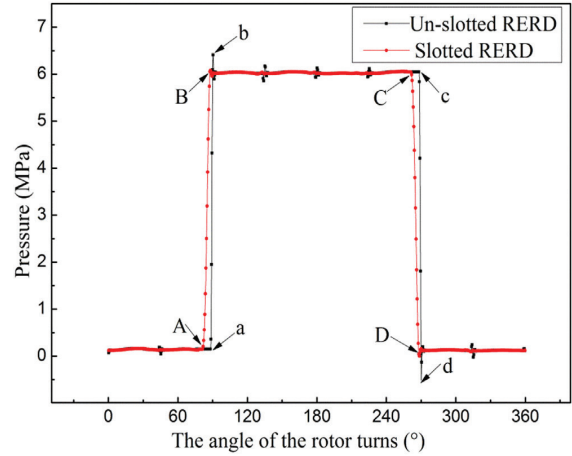
Fig. 8. Volumetric mixing of the RPE. (a) volumetric mixing with different orthogonal parameters, (b) relationship between  $Q_{LP-in}$  and volumetric mixing by Liu et al. [11].

to decrease with the increase of the gap heights between valve-port plates. This is because the flow velocity inside the valve-port plate gap with the gap height of 5 microns is higher than that of 10  $\mu m$ , 15  $\mu m$ , and 20  $\mu m$ , and the pressure inside the duct is easy to be established. During the high-pressure stage (2 ms–0.02 s), the curves become flat but exhibit some significant peaks. These pressure peaks in the duct may result from the uncontrolled expansion of

the reversed fluid and leakage flow inside the valve-port plate gap. It is evident that the pressure ripple inside the duct increases with the increase of the valve-port plate gap heights. Due to the reversed fluid through the silencing groove  $q_i$  is ten times less than the leakage in lubricating gaps  $q_l$ , the right hand of Eq. (5) is negative. As the gap height between valve-port plates increases, the leakage flow through the valve-port plate gap  $q_l$  could also increase.



(a) with different gap heights of the valve-port plate interface



(b) pressure inside the duct under different structures presented by Wang et al. [18]

Fig. 9. Pressure inside the duct. (a) with different gap heights of the valve-port plate interface, (b) pressure inside the duct under different structures presented by Wang et al. [18]

Based on Eq. (6), as the pressure difference between  $P_o$  and  $P_d$  is constant, the reversed flow  $q_i$  is unchanged. As a result, the pressure ripple inside the duct will be higher with a larger lubricating gap. As expected in Fig. 9a, during the pressure reduction stage (0.02 s–0.0212 s), the pressure inside the duct changed the same trend as that of the pressure build-up stage. As stated previously, the higher gap height between valve-port plates could reduce the flow velocity through the discharge port. Thus the pressure inside the duct decreases slowly. Fig. 9b illustrates the pressure inside the duct vs. the rotor angle drawn by Wang et al. [18]. In comparison of Fig. 9a and Fig. 9b, it is visible that the variation tendency of the pressure inside the duct in this study is consistent with the calculation result by Wang et al. [18]

Fig. 10 shows the discharge flow of RPE  $Q_{HP-out}$  with different gap heights of the valve-port plate interface. The flow ripple rate of RPE is 6.15%, 10.28%, 17.77%, 36.13% with the gap heights of 5, 10, 15 and 20  $\mu\text{m}$ . That is to say, the flow ripple increased with the increase of the gap heights between valve-port plates within a certain range. Moreover, the energy recovery efficiency  $E$  of PRE is 97.2%, 82.3%, 70.5%, 49.8% with the gap heights of 5, 10, 15 and 20  $\mu\text{m}$ . This is due to the fact that the larger gap height could increase the leakage flow through the valve-port plate gaps, and decrease the flow of pressurized seawater at high pressure outlet. And then, the energy recovery efficiency  $E$  of RPE is expected to be decreased.

### 3.4. Effect of gap heights between valve-port plates on flow characteristics of IERPBD

Based on the previous research, a set of optimal parameters was determined for the REP and IERPBD. To investigate the sensitivity of the flow characteristics of IERPBD to the different gap heights between valve-port plates, the simulations are performed at the gap heights of 10 and 15  $\mu\text{m}$ , respectively. Fig. 11 represents the pressure  $P_p$

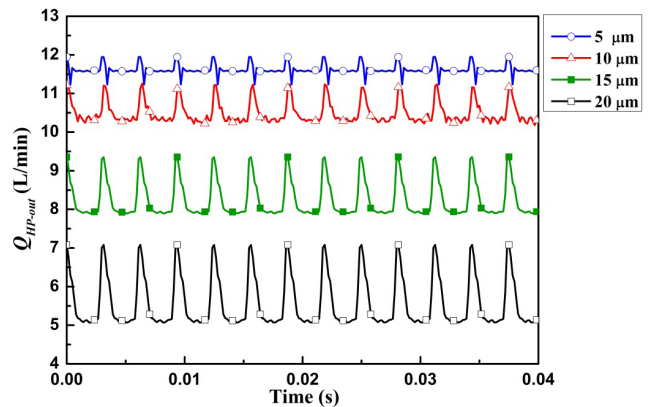


Fig. 10. Discharge flow of the RPE with different gap heights of the valve-port plate interface.

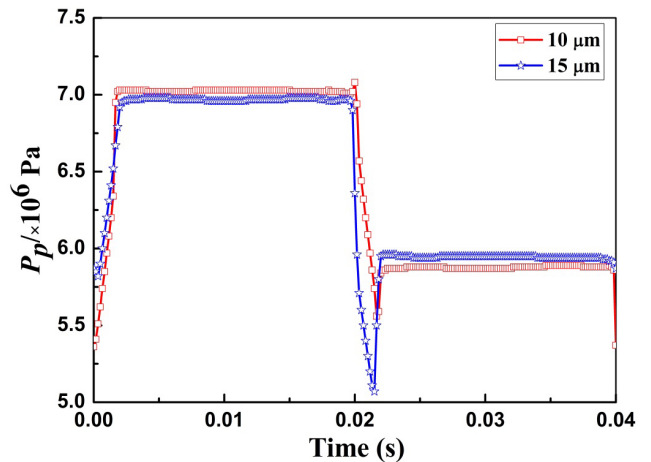


Fig. 11. Pressure inside the piston chamber of IERPBD with different gap heights of the valve-port plate interfaces.

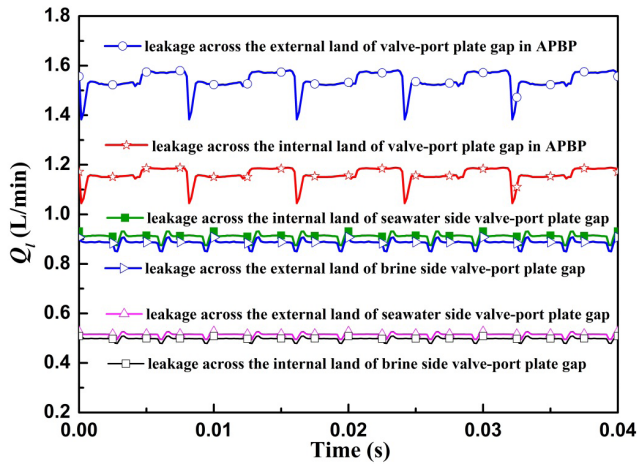


Fig. 12. Leakage flow through the valve-port plate interfaces.

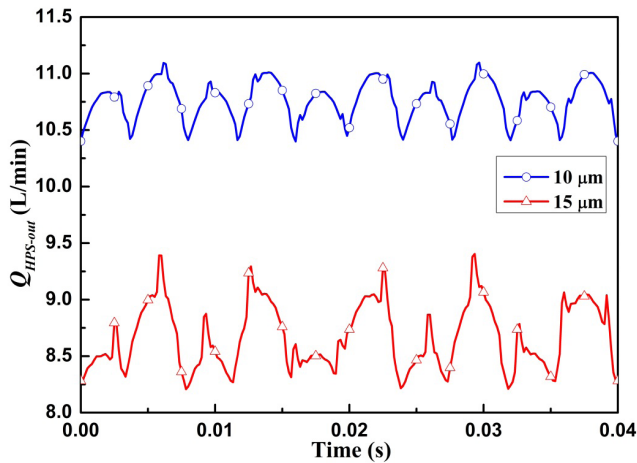


Fig. 13. Discharge flow of the IERPBD with different gap heights of the valve-port plate interface.

inside the piston chamber of the IERPBD with different gap heights between the valve-port plate interfaces. It can be seen from Fig. 11 that the  $P_p$  is mainly ranged from 5.0 to 7.0 MPa, and the amplitude of the pressure ripple during the pressure build-up stage with the gap height of 10  $\mu$ m is higher than that of 15  $\mu$ m. Fig. 12 displays the leakage flow  $Q_i$  through the different valve-port plate gaps of IERPBD. It is noteworthy from Fig. 12 that the leakage flow across the external land of valve-port plate gap is higher than that of the internal land of the valve-port plate gap. Moreover, the number of pulsations of the RPE and APBP is identical to the number of ducts and pistons. Fig. 13 illustrates the discharge flow of IERPBD  $Q_{HPS-out}$  with different gap heights between the valve-port plate interfaces. It was evident from Fig. 13 that the leakage and flow ripple rate of the IERPBD increased along with the increase of gap height between valve-port plates. This is because the flow ripple of the IERPBD consists of the reversed flow through the silencing groove and the fluid elastic ripple. Moreover, a sudden communication between the larger valve plate gap and port plate port could result in the higher pressure overshoot and undershoot inside the piston chamber.

#### 4. Conclusions

The flow, pressure, and energy transfer characteristics of the IERPBD with silencing grooves under different structure and operating parameters have been studied in this research. And both the structure parameters and working conditions of the integrated energy recovery and pressure boost device have been optimized. The numerical results are validated by comparison to the studies by Liu et al. [11] and Wang et al. [18]. As a result, the following conclusions can be obtained.

(1) The CFD simulation model of the integrated energy recovery and pressure boost device with different structure and operating parameters including duct diameter, duct length, number of ducts, gap heights between valve-port plates and fresh seawater flow has been developed, which contains the silencing grooves and lubricating gaps between valve-port plates in the rotary pressure exchanger and axial piston type booster pump. The effects of fluid compressibility and cavitation damage are considered in this three-dimensional CFD simulation.

(2) The structure and operating parameters of the rotor have a noticeable influence on the maximum rotor inflow length, the volumetric efficiency of the duct and volumetric mixing of the rotary energy recovery device. Based on the principle of orthogonal design, the optimal structure parameters with duct diameter of 10 mm, duct length of 70 mm, number of ducts of 12 and fresh seawater flow of 10.8 L/min of the rotary pressure exchanger have been determined.

(3) The energy transfer and flow characteristics of the integrated energy recovery and pressure boost device are related with the gap heights between valve-port plates. As the gap heights between valve-port plates increases from 5  $\mu$ m to 20  $\mu$ m, the energy recovery efficiency of the rotary pressure exchanger could be decreased 97.2% to 49.8%. Moreover, the flow ripple and pressure ripple inside the duct and piston chamber of the integrated energy recovery and pressure boost device increased with the increase of the gap heights between valve-port plates within a specific range.

In order to further optimize the characteristic parameters and improve the flow, pressure and energy transfer characteristics of the integrated energy recovery and pressure boost device, the device prototype will be manufactured, and an experimental study for validating the CFD simulation results will thus be one of the main research concerns in the future.

#### Acknowledgments

The authors would like to thank the Beijing Natural Science Foundation (Grant Nos. 1184012, 3182003 and 3164039), National Natural Science Foundation of China (Grant Nos. 51705008 and 11572012), Beijing Municipal Science and Technology Project (Grant No. KM201810005014), China Postdoctoral Science Foundation funded project (Grant No. 2017M620551) and Beijing Postdoctoral Research Foundation (Grant No. 2017-ZZ020) for their funding for this research. The authors are very grateful to the editors and the anonymous reviewers for their insightful comments and suggestions.

## Symbols and abbreviations

$l_{\max}$	— The maximum rotor inflow length (mm)
$\eta$	— Volumetric efficiency of the duct (%)
$\varphi$	— Volumetric mixing ratio (%)
$E$	— Energy recovery efficiency (%)
$t_0$	— Sealing time of the duct (s)
$T$	— Rotating period of the rotor (s)
$v_{\text{mix}}(t)$	— Velocity of the fluid in the duct (m/s)
$L$	— Length of the duct (mm)
$C_{\text{HP-out}}$	— Salinity of the pressurized seawater at high-pressure outlet (%)
$C_{\text{LP-in}}$	— Salinity of fresh seawater at low-pressure inlet (%)
$C_{\text{HP-in}}$	— Salinity of incoming brine at high-pressure inlet (%)
$P_{\text{HP-out}}$	— Pressure of pressurized seawater at high-pressure outlet (MPa)
$P_{\text{HP-in}}$	— Pressure of high-pressure brine at high-pressure inlet (MPa)
$P_{\text{LP-in}}$	— Pressure of the fresh seawater at low-pressure inlet (MPa)
$Q_{\text{HP-out}}$	— Flow of pressurized seawater at high-pressure outlet (L/min)
$Q_{\text{HP-in}}$	— Flow of high-pressure brine at high-pressure inlet (L/min)
$Q_{\text{LP-in}}$	— Flow of the fresh seawater at low-pressure inlet (L/min)
$Q_l$	— Leakage flow through the valve-port plate gap (L/min)
$Q_{\text{HPS-out}}$	— Discharge flow of IERPBD (L/min)
$P_d$	— Temporal pressure inside duct (MPa)
$P_p$	— Temporal pressure inside piston chamber (MPa)
$K_e$	— Bulk modulus of the fluid (Pa)
$V$	— Temporal volume of duct (L)
$q_i$	— Reverse flow through the silencing groove (L/min)
$q_l$	— Leakage from gap between valve plate and port plate (L/min)
$C_i$	— Discharge coefficient of the silencing groove
$A_i$	— Flow area of the silencing groove (mm <sup>2</sup> )
$P_0$	— Outlet pressure at high-pressure outlet (MPa)
$\rho$	— Density of the fluid (Kg/m <sup>3</sup> )
$\Omega(t)$	— Control volume (mm <sup>3</sup> )
$\sigma$	— Surface area of control volume (mm <sup>2</sup> )
$v, v_\sigma$	— Fluid velocity vector and the surface motion velocity vector (m/s)
$N$	— Normal vector of point on surface
$p$	— Fluid pressure (Pa)
$F$	— Body force (N)
$\tau$	— Shear stress tensor
$\delta_{ij}$	— Kronecker delta function
$\mu_1$	— Dynamic viscosity of brine (Pa·s)
$\mu_2$	— Dynamic viscosity of seawater (Pa·s)
$\rho_1$	— Density of brine (Kg/m <sup>3</sup> )
$\rho_2$	— Density of seawater (Kg/m <sup>3</sup> )
$T_i$	— Operating Temperature (°C)
$n$	— Rotational speed (r/min)
$N$	— Number of ducts
$\delta$	— Height of the valve-port plate lubricating gap (mm)

## References

- [1] Y. Lu, Y.Y. Zhao, G.X. Bu, P.C. Shu, The integration of water vane pump and hydraulic vane motor for a small desalination system, *Desalination*, 276 (2011) 60–65.
- [2] H.Y. Yang, M. Pan, Engineering research in fluid power: a review, *J. Zhejiang Univ. Sci., A*, 16 (6) (2015) 427–442.
- [3] L.S. Drabløs, Testing of danfossAPP1.0-2.2 with APP pumps as water hydraulic motors for energy recovery, *Desalination*, 183 (2005) 41–54.
- [4] A. Farooque, A. Jamaluddin, A.R. Al-Reweli, P. Jalaluddin, S. Al-Marwani, A. Al-Mobayed, A. Qasim, Comparative study of various energy recovery devices used in swro process, *Saline Water Desalination Research Institute, Saline Water Conversion Corporation (SWCC)*, 2004.
- [5] N. Liu, Z.L. Liu, Y.X. Li, L.X. Sang, Studies on leakage characteristics and efficiency of a fully-rotary valve energy recovery device by CFD simulation, *Desalination*, 415 (2017) 40–48.
- [6] N. Liu, Z.L. Liu, Y.X. Li, L.X. Sang, Development and experimental studies on a fully-rotary valve energy recovery device for SWRO desalination system, *Desalination*, 397 (2016) 67–74.
- [7] F.H. Ye, J.Q. Deng, K. Liu, Z. Cao, Performance study of a rotary vane pressure exchanger for SWRO, *Desal. Water Treat.*, 89 (2017) 36–46.
- [8] I.B. Cameron, R.B. Clemente, SWRO with ERI's PX pressure exchanger device-aglobal survey, *Desalination*, 221 (2008) 136–142.
- [9] R.L. Stover, Seawater reverse osmosis with isobaric energy recovery devices, *Desalination*, 203 (2007) 168–175.
- [10] Y. Zhou, X. Ding, M. Ju, Y. Chang, Numerical simulation on a dynamic mixing process in ducts of a rotary pressure exchanger for SWRO, *Desal. Water Treat.*, 1 (2009) 107–113.
- [11] Y. Liu, Y.H. Zhou, M.S. Bi, 3D numerical simulation on mixing process in ducts of rotary pressure exchanger, *Desal. Water Treat.*, 42 (2012) 269–273.
- [12] F. Zhao, Z.M. Feng, L. Jiao, C.J. Wu, Z.X. Zhang, C.P. Zhao, S.B. Yao, The analysis of pressure fluctuation frequency with rotor rotation speed in pressure exchanger, *J. Eng. Therm.*, 35 (2014) 74–77.
- [13] W.J. Yuan, J.Q. Deng, Z. Cao, Dynamic length research on the pulsating mixing of rotary pressure exchanger, *J. Eng. Therm.*, 36 (2015) 766–769.
- [14] Y. Wang, L.Y. Wu, B. Li, W.T. Zhang, Y.D. Hu, Numerical simulation and analysis of the mixing process of rotary pressure exchangers with different sizes and structures, *J. Chem. Eng. Jpn.*, 49 (2016) 573–578.
- [15] Z. Cao, J.Q. Deng, W.J. Yuan, Z.H. Chen, Integration of CFD and RTD analysis in flow pattern and mixing behavior of rotary pressure exchanger with extended angle, *Desal. Water Treat.*, 57 (2016) 15265–15275.
- [16] E. Xu, Y. Wang, L. Wu, S. Xu, Y. Wang, S. Wang, Computational fluid dynamics simulation of brine-seawater mixing in a rotary energy recovery device, *Ind. Eng. Chem. Res.*, 53 (2014) 18304–18310.
- [17] E. Xu, Y. Wang, J. Wu, S. Xu, S. Wang, Investigations on the applicability of hydrostatic bearing technology in a rotary energy recovery device through CFD simulation and validating experiment, *Desalination*, 383 (2016) 60–67.
- [18] Y. Wang, Y.W. Duan, J. Zhou, S.C. Xu, S.C. Wang, Introducing pre-pressurization/depressurization grooves to diminish flow fluctuations of a rotary energy recovery device: Numerical simulation and validating experiment, *Desalination*, 413 (2017) 1–9.
- [19] E. Xu, Y. Wang, J. Zhou, S.C. Xu, S.C. Wang, Theoretical investigations on rotor speed of the self-driven rotary energy recovery device through CFD simulation, *Desalination*, 398 (2016) 189–197.
- [20] R.L. Stover, Development of a fourth generation energy recovery device. A 'CTO's notebook', *Desalination*, 165 (2004) 313–321.
- [21] D.Z. Wu, J. Wu, F. Zhao, T.C. Miao, C.J. Wu, L.Q. Wang, The research on internal leakage and lubrication property of gap in rotary pressure exchanger, *J. Chem. Eng. Chin. Univ.*, 28 (2014) 1204–1209.

- [22] L.M. Wu, Y. Wang, E.L. Xu, J.N. Wu, S.C. Xu, Employing groove-textured surface to improve operational performance of rotary energy recovery device in membrane desalination system, *Desalination*, 369 (2015) 91–96.
- [23] J.N. Wu, Q. Jin, Y. Wang, P. Tandon, Theoretical analysis and auxiliary experiment of the optimization of energy recovery efficiency of a rotary energy recovery device, *Desalination*, 415 (2017) 1–7.
- [24] R.L. Stover, B. Andrews, Isobaric energy-recovery devices: past, present, and future, *J. Water Reuse Desal.*, 4 (2012) 38–43.
- [25] V. Pikalov, S. Arrieta, A.T. Jones, J.L. Mamo, Demonstration of an energy recovery device well suited for modular community-based seawater desalination systems: Result of Danfoss iSAVE 21 testing, *Desal. Water Treat.*, 51(22–24) (2013) 4694–4698.
- [26] D.F. Wu, Y.S. Liu, D.L. Li, X.F. Zhao, C. Li, Effect of materials on the noise of a water hydraulic pump used in submersible, *Ocean Eng.*, 131 (2017) 107–113.
- [27] F.L. Yin, S.L. Nie, H. Ji, Y.Q. Huang, Non-probabilistic reliability analysis and design optimization for valve-port plate pair of seawater hydraulic pump for underwater apparatus, *Ocean Eng.*, 163 (2018) 337–347.
- [28] F.L. Yin, S.L. Nie, W. Hou, S.H. Xiao, Effect analysis of silencing grooves on pressure and vibration characteristics of seawater axial piston pump, *P. I. Mech. Eng. C-J.Mec.*, 231 (8) (2017) 1390–1409.
- [29] J.M. Bergada, S. Kumar, D.L. Davies, J. Watton, A complete analysis of axial piston pump leakage and output flow ripples, *Appl. Math Model.*, 36 (2012) 1731–1751.
- [30] H. Ding, F.C. Visser, Y. Jiang, M. Furmanczyk, Demonstration and validation of a 3D CFD simulation tool predicting pump performance and cavitation for industrial applications, *ASME J. Fluids Eng.*, 133 (2011) 011101.
- [31] S.G. Ye, J.H. Zhang, B. Xu, W. Song, L. Chen, H.Y. Shi, S.Q. Zhu, Experimental and numerical studies on erosion damage in damping holes on the valve plate of an axial piston pump. *J Mech Sci Technol.*, 31(2017) 4285–4295.
- [32] N.D. Manning, Y.H. Zhang, The improved volumetric-efficiency of an axial piston pump utilizing a trapped-volume design, *ASME J. Dyn. Syst., Meas., Control*, 123 (2001) 479–487.